THE ASTRONOMICAL JOURNAL VOLUME 105, NUMBER 4 APRIL 1993

A MAXIMUM-LIKELIHOOD ANALYSIS OF GLOBULAR CLUSTER LUMINOSITY DISTRIBUTIONS IN THE VIRGO ELLIPTICALS

JEFF SECKER AND WILLIAM E. HARRIS
Department of Physics and Astronomy, McMaster University, Hamilton, Ontario, Canada L8S 4M1

Received 1992 October 29; revised 1992 December 11

ABSTRACT

We have formulated a model to represent globular cluster luminosity functions (GCLFs) in distant galaxies by means of maximum-likelihood statistics. This model simultaneously accounts for the presence of a contaminating background population, incompleteness at faint magnitudes, and photometric measurement error. We apply this model to observational data sets for the three Virgo giant elliptical galaxies NGC 4365, 4472, and 4649, to derive accurate new values for the GCLF peak and dispersion. With a Virgo core distance modulus of $(m-M)_V=30.95\pm0.25$, we obtain GCLF turnover luminosities for the three gEs as follows: $M_V^0=-7.12\pm0.36$ and $\sigma_t=1.52\pm0.13$ (NGC 4365), $M_V^0=-7.03\pm0.27$ and $\sigma_t=1.30\pm0.07$ (NGC 4472), and $M_V^0=-7.18\pm0.27$ and $\sigma_t=1.15\pm0.07$ (NGC 4649). Accordingly, the unweighted average of these GCLF parameter estimates are $\langle M_V^0\rangle=-7.11\pm0.3$ and $\langle\sigma_t\rangle=1.32\pm0.09$. Comparing with similar maximum-likelihood parameter estimates for M31 and the Milky Way, we obtain mean differences $\Delta M_V^0=-0.31\pm0.33$ mag and $\Delta\sigma_t=-0.36\pm0.13$ mag, in the sense that the GCLFs in the giant ellipticals are slightly less luminous at the turnover but with significantly large functional dispersion.

1. INTRODUCTION

The analysis of globular cluster systems (GCSs) in the halos of galaxies of different morphologies can tell us a great deal about the earliest periods of star formation in galaxies. One prominent and easily measured characteristic of the GCS is the globular cluster luminosity function (GCLF), which we define here as the probability of observing a globular cluster at a given magnitude. (In this paper, we write LF when referring to a luminosity function other than the GCLF, e.g., the magnitude distribution of stars and faint galaxies.) Analysis of the GCLF is important from the perspectives of (a) distance estimation (i.e., the GCLF itself is taken to be a "standard candle") and (b) galaxy formation models and the dynamical evolution of the GCS. The first-order similarity of the GCLF from galaxy to galaxy has become increasingly well justified from a purely observational viewpoint (e.g., Harris 1991). The physical processes which might have dictated the formation and evolution of a "universal" GCLF are not yet completely understood, but several possibilities on theoretical grounds now exist (e.g., Fall & Rees 1988; Jacoby *et al.* 1992; Harris 1991; Pudritz & Harris 1993).

For galaxies within the Local Group (M31, the Milky Way, the dwarf ellipticals), there are now well-defined samples of globular clusters that are complete to faint absolute magnitudes and uncontaminated by other types of objects (Harris *et al.* 1991, hereafter HAPV; Reed *et al.* 1992; Racine & Harris 1992; Secker 1992). Though none of these samples contains more than $\sim$100 clusters, they act as the primary GCLF calibrators to which all other GCSs in distant galaxies must be compared. For galaxies more distant than about 5 Mpc, however, two new observational problems enter the picture when one attempts to define a GCLF for a given galaxy: (a) the globular clusters appear starlike at any ground-based image resolution, so that the total cluster population must be deduced as a statistical excess above the surrounding background of starlike objects (foreground stars and faint, small background galaxies); and (b) photometric incompleteness and measurement uncertainty cut off the definition of the GCLF at faint limits. The traditional way to extract the underlying shape of the GCLF in such galaxies has been to start with the raw LF of all objects around the galaxy, subtract off the background LF, correct for photometric incompleteness, and then fit some fiducial curve (usually a Gaussian) to the magnitude-limited partial GCLF that remains after these corrections. The best-fit criterion may be established by simple least squares (HAPV) or by a restricted maximum-likelihood approach (Hanes & Whittaker 1987).

In this paper we formulate some improved methodology, based on a fuller use of maximum-likelihood fitting, to determine the intrinsic parameters describing the GCLF, which are specifically designed to address the problems mentioned above. We then apply these techniques to the GCSs around three of the Virgo giant elliptical galaxies, using the data samples published in HAPV. As will be seen below, these lead to improved definitions of the GCLF parameters (the turnover luminosity and dispersion), as well as better definitions of their fundamental uncertainties. Finally, we present a revised comparison of the Virgo GCLF samples with those of M31 and the Milky Way, and their application to the distance scale.

2. THE DATA SAMPLE

The Virgo Cluster galaxies provide a natural testbed for our study, since the GCS populations for the central gEs there are very large (the sample sizes can be as large as

 0004-6256/93/041358-11$00.90

TABLE 1. Properties of the CCD fields.

Field	Area (arcmin^2)	N
N4365	5.75	584
N4472	11.90	1187
N4649	6.37	643
B1	7.08	301
B2	7.18	321
B1B2	14.26	622

thousands of clusters per galaxy), there is no problem with foreground reddening, and they are at a small enough distance that the GCLF can be observed directly to levels fainter than the "turnover" (peak frequency of the GCLF). In essence, the Virgo Cluster therefore provides the most important laboratory in which to define the GCLF properties for giant elliptical galaxies and to link them with the Local Group calibrators.

In this paper, a parameter estimation method is developed in order to analyze the GCLFs for three particular Virgo galaxies, NGC 4365, 4472, and 4649. The data for these are taken from a previous study (HAPV). The analytic fitting method they used to estimate the GCLF turnover and dispersion has several inherent limitations: it employs a simple least-squares fit to the binned residual LF only after correction for photometric faint-end incompleteness and background subtraction, and does not utilize the complete data set, i.e., down to the very faintest objects detectable. They suggest that a more general maximum-likelihood probability contour approach would be more appropriate, in which the Virgo cluster distribution and the background are modeled simultaneously, and in which the parametric model GCLF is fit directly to the *raw* data. In Secs. 3 and 4 we develop the statistical framework necessary to perform this simultaneous modeling and the subsequent parameter estimation.

The database, as described in HAPV and in Pritchet & van den Bergh (1987), consists of images of fields around these three ellipticals obtained at the Canada–France–Hawaii Telescope (CFHT) in *B*. Two background fields, adjacent to NGC 4365 (labeled B1) and 4649 (labeled B2), were also imaged on additional nights during the same observing run, to similar photometric limits. Image classification (see HAPV) was applied uniformly to all the galaxy and control fields in order to eliminate most of the nonstellar objects from the lists and thus reduce the background contamination. In Table 1, using data drawn from HAPV, we summarize the characteristics of these fields which are relevant to our study. In this and future tables and figures, B1B2 refers to the summation of the two control fields, and N gives the number of starlike objects measured in each data set.

3. STATISTICAL FORMULATION

3.1 The Distribution Model

The basis of our method is to formulate a distribution function which will correctly model the photometry of the observed galaxy field LF (i.e., the GCLF plus background). This distribution function must also account for the effects of incompleteness and measurement uncertainty on the observed data set. The simultaneous distribution function defined by the incorporation of these effects will by definition model the raw, observed data set. The GCLF intrinsic parameters will be extracted from the observed data set by using maximum-likelihood techniques to generate probability contours. We define the simultaneous distribution function $\phi(m)$, the probability of observing an object a magnitude m in the raw data set as,

$$\phi = KI \cdot (\epsilon \circ \gamma) + (1-K)\beta, \tag{1}$$

where β, ϵ, and γ are functions of magnitude m, and represent the background, measurement uncertainty, and intrinsic GCLF distribution functions, respectively. Also, $I(m)$ represents the completeness function (i.e., the probability that an object of magnitude m would be detected in the measurement process), K is a scaling factor for the relative contribution of the GCLF and the background LF distributions, and $(\epsilon \circ \gamma)$ denotes a convolution product. It is clear that as long as β and $I(\epsilon \circ \gamma)$ are normalized to a sum of unity over the entire magnitude range, ϕ will also be.

For this study, we assume that the incompleteness function is the same for both the background and galaxy fields, an assumption which is very nearly true for the Virgo data that we use here. However, this assumption is not a requirement (cf. Sec. 4).

In Eq. (1), $\gamma(m)$ represents the function whose (initially unknown) parameters must be deduced from the fitting process, whereas the background β, error ϵ, and incompleteness I are known beforehand directly from the reduction of the observations. It should be noted that the $I(\epsilon \circ \gamma)$ term of (1) could also be represented as $\epsilon \circ (I\gamma)$. Either may be argued as correct, but the former was chosen for this paper, and the effects of this choice will be of second order and therefore negligible. Each of the components in the above simultaneous distribution function will be discussed in detail below.

3.2 The GCLF Distribution Function

Our study of the Virgo GCLFs is aided by using a suitable analytic form of the GCLF; that is, a function which matches the most probable form of the true underlying distribution function. This gives us an extremely convenient method for describing the main features of the GCLF and (more importantly) comparing them in different galaxies. Recent studies of the Milky Way and M31 demonstrate that the form of the GCLF is unimodal and nearly symmetric, though in the past it has been assumed specifically that the shape of the GCLF is well described by a Gaussian (e.g., Hanes 1977; Harris & Racine 1979; van den Bergh 1985; Hanes & Whittaker 1987; HAPV). It was shown in Secker (1992) that a t distribution with a shape parameter of $\mu = 5$ is a two-parameter function which is as simple as the traditional Gaussian, slightly more successful at fitting both the Milky Way and M31 data sets, and more

robust against outliers and small asymmetries in the data. The form of this t_5 distribution function is given by

$$\gamma(m)=\frac{8}{3\sqrt{5\pi}\sigma_t}\left(1+\frac{(m-m^0)^2}{5\sigma_t^2}\right)^{-3}, \quad (2)$$

where the two free parameters are the *peak frequency* or turnover m_0 and the *dispersion* σ_t. This is the form that we will use here to model the Virgo GCLFs. The dispersion of the t_5 function is in theory related to the Gaussian dispersion by $\sigma_G \simeq 1.29\sigma_t$, though in practice individual data sets may vary substantially from this. Secker (1992) found that the most probable t_5 parameters characterizing the Milky Way GCLF are $M_V^0=-7.29\pm0.13$ for the peak, and $\sigma_t=1.1\pm0.1$ mag for the dispersion parameter; and for M31, $V^0=17.00\pm0.11$ and $\sigma_t=0.82\pm0.08$ for the peak and dispersion. Adopting the van den Bergh (1991) M31 true distance modulus $(m-M)_0=24.3\pm0.1$ (i.e., 725 ± 35 kpc) and $E_{B-V}(\mathrm{M31})=0.08$ (Burstein & Heiles 1984), we obtain $M_V^0(\mathrm{M31})=-7.55\pm0.15$, a value slightly more luminous than for the Milky Way. These quantities will be used to compare with the Virgo ellipticals once solutions for them have been performed in the same manner.

3.3 The Background Luminosity Function

The background LF $\beta(m)$ comprises the sum of the foreground stars plus whatever (near-starlike) faint background galaxies remained in the sample after the image classification was done (see HAPV). This function can be given in either a parametric or nonparametric form, and we adopt the latter approach to match the raw data as closely as possible. This was done using the generalized histogram approach outlined (for example) in Searle & Zinn (1978). For each of the $i=1,\ldots,N$ images in the background field, we define a unit Gaussian centered at $\{m_i\}$, where the uncertainty in the magnitudes is reflected by the Gaussian dispersion which is used. In this paper (for both the simulations and data analysis), we used a Gaussian dispersion of 0.1 mag, which proved to match the observed background LFs accurately without too large a smoothing effect. Then the summation of these N unit Gaussians, with the proper $1/N$ normalization factor, yielded the nonparametric probability distribution function $\beta(m)$, representing the background field LF. The calculated background distribution functions are plotted in Fig. 1, superimposed for illustration purposes on the *binned* background LF (although we stress once again that we do not use any form of binned data in the functional fits below).

3.4 The Completeness Function

The completeness function $I(m)$ expresses the probability that an object at a given magnitude m will be detected (in this case, by the DAOPHOT/FIND algorithm of Stetson 1987, but the same principle applies to any automated photometry code). Knowing $I(m)$ accurately is essential for modelling the Virgo GCLFs, since we can then use it to model the complete range of data down to the faintest objects measured. The completeness functions for

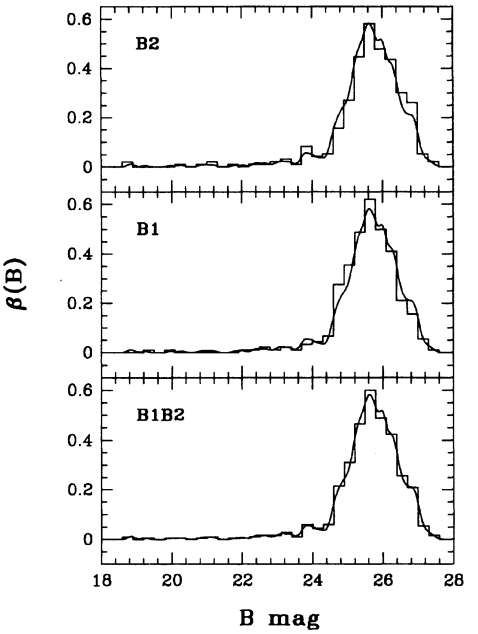

FIG. 1. The probability distribution functions $\beta(m)$ representing the background field LFs. These are illustrated here as the solid lines superimposed upon an appropriately scaled histogram of the actual background field data (0.3 mag bins). The $\beta(m)$ are nonparametric, digital functions, generated from the B1, B2, and B1 plus B2 (i.e., B1B2) data sets using the generalized histogram method (cf. Sec. 3.3), with a Gaussian smoothing dispersion of 0.1 mag.

TABLE 2. Completeness data for galaxy fields.

B	I(B)		
	NGC 4365	NGC 4472	NGC 4649
23.5	1.00	1.00	1.00
23.7	1.00	1.00	1.00
23.9	1.00	0.99	0.99
24.1	1.00	0.97	0.98
24.3	1.00	0.96	0.97
24.5	0.99	0.94	0.96
24.7	0.98	0.92	0.94
24.9	0.97	0.90	0.92
25.1	0.96	0.87	0.90
25.3	0.95	0.84	0.88
25.5	0.91	0.79	0.84
25.7	0.86	0.74	0.80
25.9	0.78	0.64	0.73
26.1	0.55	0.48	0.63
26.3	0.38	0.27	0.47
26.5	0.22	0.13	0.30
26.7	0.13	0.04	0.16
26.9	0.05	0.00	0.06
27.1	0.00	0.00	0.00
27.3	0.00	0.00	0.00

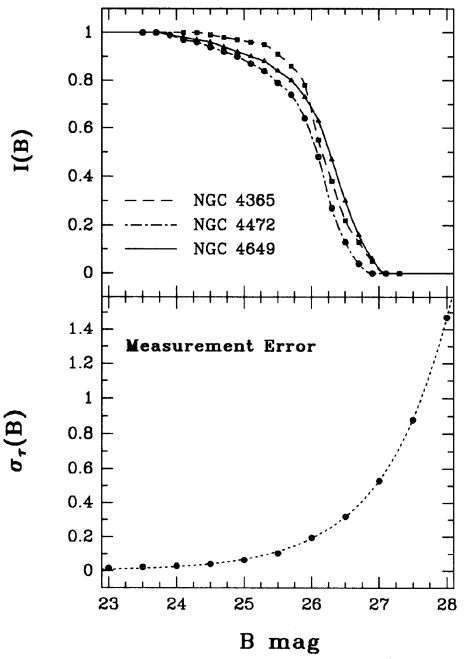

FIG. 2. Completeness functions and measurement errors. (a) Top panel: the completeness data (Table 2) for the three Virgo giant elliptical galaxies, together with the interpolated results. Note that all galaxy fields have a zero completeness level for $B \gtrsim 27$ mag. (b) Bottom panel: dispersion of the measurement uncertainty $\sigma_\tau(m)$ vs B (refer to Table 2 of HAPV for the actual data). In this magnitude range, the relation is well approximated by an exponential function, as indicated by the hatched line. The general level of σ_τ is so low because the galaxy fields are averages of the median images for many nights of observing (cf. HAPV).

the Virgo CCD fields are given in Table 2, derived through artificial-star experiments as described in HAPV. Note that we have extended the completeness curves to fainter magnitudes than were listed in HAPV, using the relevant unpublished data from their work.

In order to use the data in Table 2 for our calculations, it is necessary to be able to interpolate between the known values for any required (i.e., observed) data value. We chose to use a one-dimensional monotonic interpolation method (Steffen 1990), based on a third-order polynomial passing through the data points in each small region. This procedure guarantees a smooth curve with continuous first derivatives passing through the given set of data points, without the spurious oscillations which often arise from techniques such as cubic-spline interpolations. The interpolated $I(m)$ values are stored in an array covering the complete range of observed B data with a mesh size of $\Delta m = 0.01$ mag, ample for our calculation purposes. The data in Table 2 are shown in the upper graph of Fig. 2 together with the interpolation curves. For this analysis it is not necessary that the completeness function have continuous first derivatives, just that it is defined at all magnitudes. Therefore we can extrapolate on both ends of the interpolated function (i.e., at either zero or unity) and not worry about kinks or discontinuities in the derivatives.

3.5 Photometric Measurement Uncertainty

Even in the absence of any contaminating background LF, the GCLF in a distant galaxy will not appear to the observer exactly as described by the GCLF distribution function (2), because the observations will be affected by a multitude of different random measurement errors that become progressively more important at fainter levels. In our model [i.e., Eq. (1)], we account for this measurement error by convolving the expected GCLF, $\gamma(m)$, with an appropriate "smearing function," $\epsilon(m)$. For this paper we represent the measurement error $\epsilon(m)$ by a Gaussian function with a total dispersion σ_τ. That is, we have

$$\epsilon_{m_i}(m) = \frac{1}{\sqrt{2\pi}\sigma_\tau} \exp\left(-\frac{(m-m_i)^2}{2\sigma_\tau^2}\right), \quad (3)$$

where σ_τ is itself a function of magnitude m_i. We note that $\epsilon(m)$ need not be a Gaussian or even any other analytic function, and therefore the form of (3) is not essential to our model. This flexibility in our formulation is possible because we use maximum-likelihood methods for parameter estimation as opposed to the methods of least squares.

To perform the convolution $\epsilon(m) \circ \gamma(m)$, a tabulated list of σ_τ for the complete magnitude range is required. We adopted the $\sigma_\tau(m)$ relation as given by HAPV, and this is plotted here in the lower graph of Fig. 2; it is very similar for all the observed fields. For the calculations in this paper, it was necessary to both interpolate and extrapolate upon the measurement error data. Using the interpolation method of Steffen described in Sec. 3.4, a look-up table for σ_τ in the range of $22.0 \lesssim B \lesssim 26.5$ was created. For the brighter magnitudes (i.e., $B < 22.0$), the measurement error was assumed to remain constant at the lower limit of 0.012 mag. For the fainter magnitudes (i.e., $B > 26.5$), the measurement error was estimated using the least-squares determined best-fit exponential curve, given by $\sigma_\tau(B) = \exp[p(B-q)]$, with $p = 1.019$ and $q = 27.622$. The solid line in Fig. 2(b) illustrates the fit of this exponential function to the σ_τ vs B data set. Although extrapolation past the limits of the observations is not generally good practice, we have done this only because we have useful models which tell us what these functions are likely to do outside of the range of the given data, and because the very faint end of the data set exerts little influence on the total fit (see below).

Finally, we numerically convolve the measurement error $\epsilon(m)$ with the expected GCLF distribution $\gamma(m)$ using a modified version of the generalized histogram method. The probability to observe a star in the magnitude interval dm centered on m_i is given by the rectangular region $\gamma(m_i)dm$, where the probability $\gamma(m_i)$ is defined by Eq. (2) with the GCLF intrinsic parameters m^0 and σ_t. The effect of the measurement error is to smear this rectangular probability into the shape of the error function (conserving probability), $\epsilon_{m_i}(m_i)$, given by Eq.(3), where $\epsilon_{m_i}(m_i)$ is

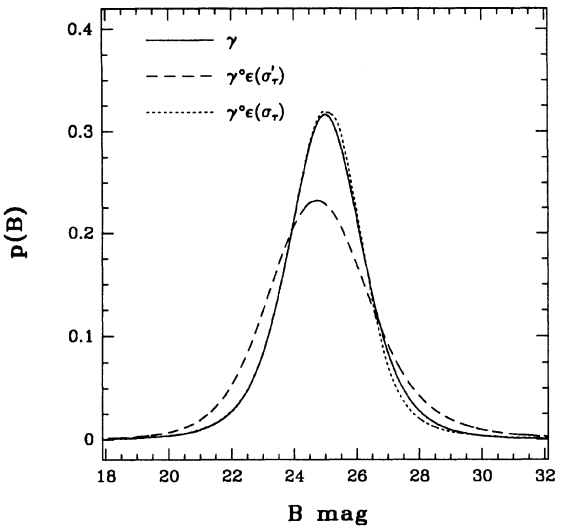

FIG. 3. Illustrated here is the effect of the total measurement uncertainty on the expected GCLF. The solid line represents the model GCLF, and the dashed lines represent two cases of convolution products. The short dashed line illustrates the minimal effect that our actual photometric error [i.e., $\sigma_\tau(m)$] has upon GCLFs of the type expected for the Virgo cluster, and the long dashed line illustrates the effect of an exaggerated measurement error [i.e., we used here $\sigma'_\tau(m)=2\sigma_\tau(m)+1$]. Note the shift in the peak, the increased dispersion and the skewed nature of this latter convolution.

normalized and centered at m_i with dispersion $\sigma_\tau(m_i)$. We denote this differential distribution function by $\delta(m_i)$, which is given by

$$\delta(m_i)=\epsilon_{m_i}(m_i)\gamma(m_i)dm. \tag{4}$$

These differential contributions to the convolution product are calculated over the complete GCLF magnitude range with $dm=0.01$ mag, and then summed together to obtain the desired convolution product, given by

$$\epsilon\circ\gamma=\sum_{m_i=m_{\min}}^{m_{\max}}\delta(m_i). \tag{5}$$

Figure 3 illustrates how the total measurement error affects the shape of the observed GCLF. The solid line is a model GCLF of the type which we expect to find in the Virgo galaxies, with an arbitrarily chosen peak magnitude at $B=25$ mag and a dispersion of $\sigma_t=1.2$ mag. Two illustrative convolutions were performed: the first with a grossly exaggerated measurement error $\sigma'_\tau=2\sigma_\tau+1$, where σ_τ is the actual dispersion as given in Fig. 2. The resulting convolution product is slightly skewed, shows an increased dispersion (corresponding to a decreased peak height), and a shift of the GCLF peak towards the brighter magnitudes. The classic *bin jumping* effect comes into play especially on the steep rise and fall of the GCLF. The number of objects which scatter to the bright side from a bin at a magnitude m_i is proportional to the number of objects n_i in that bin, and the number of objects which scatter towards the faint side of a bin at brighter magnitude m_{i-1} is proportional to the number n_{i-1} in that bin: since $n_{i-1}<n_i$ on the rising part of the GCLF, the number of objects scattering to the bright side is not compensated for by the lesser number scattering to the faint side. The characteristic *exponentially increasing measurement error* permits the probability at bright magnitudes to undergo very little smearing, whereas the probability at faint magnitudes undergoes so much smearing that it actually contributes to the probability at the brighter magnitudes, resulting in the shifted peak and the skewed distribution.

The second convolution in Fig. 3 is represented by a short hashed line, which gives the convolution product for the actual measurement error, given in Fig. 1. It is clear that a measurement error of this level has a minimal effect on the expected GCLF. The reason for this small effect is that the GCLF dispersion is much greater than the dispersion of the smearing function over almost the entire magnitude range (i.e., $\sigma_t \gg \sigma_\tau$ for $B \lesssim 26$). The maximum deviation in probability between γ and the convolution product $(\gamma\circ\epsilon)$ occurs at $B=25.51$ mag, at which point the difference $\delta p=0.0137$. Thus the convolution product deviates significantly from the "true" GCLF at faint magnitudes only, and since the data have less weight in this region, we can safely neglect the effects of the photometric measurement uncertainties for the Virgo data in the following discussion.

4. IMPLEMENTATION BY MAXIMUM LIKELIHOOD

Equation (1) is a function of magnitude m and of three parameters: (i) the magnitude peak or turnover of the GCLF, m^0; (ii) the dispersion of the GCLF, σ_t; (iii) the normalization constant K. In general, one might solve (1) in three-dimensional parameter space for the joint maximum-likelihood estimates (where the estimates are denoted by the usual symbol, with a caret on top) of the parameters $\hat{\Theta}=(\hat{m}^0, \hat{\sigma}_t, \hat{K})$, by solving

$$\left.\frac{\partial L(\Theta)}{\partial\Theta}\right|_{\Theta=\hat{\Theta}}=0, \tag{6}$$

where $L(\Theta)$ is the logarithmic likelihood equation, given by

$$L(\Theta)=\log l(\Theta)=\sum_{i=1}^{N}\log\left[\phi(m_i)\right]. \tag{7}$$

The scaling constant K is referred to as the *weighting mixture proportion*, and it governs the relative weights given to the background and the GCLF distributions. For example, if there are 300 objects in the background field, and 900 in the galaxy field with the same area, then we should have $K=2/3$. Allowable variations in K should be at the level of the $\pm\sqrt{N}$ uncertainties in the background LF. Thus, K is the only parameter subject to a legitimate external constraint. For each of the three galaxy fields, we therefore adopted a fixed value for K, as given by the relationship

$$K=\frac{N_G-SN_B}{N_G}=1-S\frac{N_B}{N_G}, \tag{8}$$

TABLE 3. Estimates for the scale and mixture constants.

Field combination	S	$\hat{K}$
N4365 & B1	0.8121	0.5814
N4649 & B2	0.8872	0.5571
N4472 & B1B2	0.8345	0.5627
N4365 & B1B2	0.4032	0.5705
N4649 & B1B2	0.4467	0.5680

where S is the ratio of the effective area of the galaxy field to the background field, and N_G and N_B are the stellar images in the galaxy and background fields, respectively (cf. Sec. 3.6). By imposing this constraint on K and solving (6) numerically in two dimensions, the maximum-likelihood parameter estimate $\hat{\Theta}=(\hat{m}^0,\hat{\sigma}_t)$ was then fully consistent with our model and boundary condition. The values of the weighting mixture constant K are given in Table 3.

Equations (6) and (7) were solved as follows. First, a multidimensional minimization routine was used to find the minimum value of the negative log-likelihood equation in a two-dimensional parameter space. This maximum of the log-likelihood equation is equivalent to the maximum of the likelihood equation (since the logarithm function is monotone increasing), and thus yields the maximum-likelihood estimates for the most probable parameter values $\hat{m}^0$ and $\hat{\sigma}_t$. Second, $L(\Theta)$ was evaluated for a grid in parameter space (we used, 151^2 to obtain good resolution), centered on $(\hat{m}^0, \hat{\sigma}_t)$ and extending sufficiently far in all directions that the log-likelihood statistic decreases from its maximum value by $\Delta L \simeq 73$ (i.e., $e^{-73} \simeq 10^{-32}$, close to zero in FORTRAN double precision). The grid of log-likelihood values is scaled such that the maximum value at $(\hat{m}^0, \hat{\sigma}_t)$ becomes zero (with all other values therefore less than zero). We then compute the corresponding grid of likelihood values ($0 \leqslant l_{ij} \leqslant 1$, calculated from the log-likelihood grid values), which is then normalized to a total probability of 1 by dividing each grid element by the sum over the entire grid. Finally, we plot the contours which enclose fractional probabilities 0.3830, 0.6826, 0.8664, 0.9544, 0.9876, and 0.9974 (i.e., 0.5, 1, 1.5, 2, 2.5, and 3σ uncertainties) about the maximum-likelihood parameter estimates. Our FORTRAN code can be made available to interested readers upon request.

Another quantity of interest which is related to K is the true number of observed globular clusters in the frame (N_{GC}). By correcting for incompleteness, we obtain

$$N_{GC}=KN_G\left[\int_{-\infty}^{\infty} I(m)\gamma(m)dm\right]^{-1}, \tag{9}$$

where the integral over magnitude represents the observed fraction of globular clusters. In the results below, this quantity is calculated and given with the other results; however, it is not as important to this study as are the GCLF peak and dispersion (i.e., conversion of N_{GC} into a true cluster population for the entire galaxy involves a further extrapolation to the whole area of the galaxy, which may be difficult to define if the original data cover only a small area, as is the case here).

As an aside, we mention here the procedure for using Eq. (1) for a data set which has *different* completeness functions for the background field and the galaxy field. Representing the two completeness functions as $I_\beta(m)$ for the background and $I_\gamma(m)$ for the galaxy field, we then define the ratio of these completeness functions as

$$r(m)=\frac{I_\gamma(m)}{I_\beta(m)}. \tag{10}$$

The background LF $\beta(m)$ is then corrected to the completeness function for the galaxy field by computing

$$\beta^*(m)=\beta(m)r(m), \tag{11}$$

where $\beta^*(m)$, once normalized, represents the background LF for the galaxy field frame and should be used with $I_\gamma(m)$ in Eq. (1). Therefore the restriction on similar completeness functions from background field to galaxy field is to some degree removed.

In this analysis we assume that the background LF is similar, and we therefore use a fixed value of K, given by (8), for each field. In reality, the background LF cannot be *identical* between frames, and we need to determine quantitatively the uncertainty introduced by realistic fluctuations in the background LF from field to field. A strict *lower* limit to this difference is given by Poisson $\pm\sqrt{N}$ variations in the number of objects and the shape of the background LF. However, for our small CCD fields, larger non-Poisson variations in the total background counts may occur due to the clustering of faint galaxies on scales similar to the area of the frame. If our background LF is dominated by faint galaxies rather than stars, then an expression for the *upper* limit to our frame-to-frame variance in the number of background objects, as given by Peebles (1980, Eq. 45.6), is

$$\langle(N-\mathcal{N}\Omega)^2\rangle=\mathcal{N}\Omega+\mathcal{N}^2\int_\Omega d\Omega_1\, d\Omega_2\, \omega(\theta). \tag{12}$$

Here, the mean density of galaxies on the CCD frame, $\mathcal{N}$, is given by $\langle N\rangle/\Omega$, where N is the number of galaxies on a frame, and Ω is the area of the CCD field. Also, $\omega(\theta)$ is the angular two-point correlation function, and θ is the angular separation of two objects contained in differential solid angle elements $d\Omega_1$ and $d\Omega_2$.

In practice, (12) gives only an extreme upper limit to the variance, since the image classification procedure already removed a large fraction of the background galaxies (especially for $B<24.5$; see HAPV). We proceeded to determine $\omega(\theta)$ using the Monte Carlo estimator, described by Hewett (1982), which is given by

$$\hat{\omega}(\theta)=\frac{N_p(\theta)}{N_r(\theta)}-1, \tag{13}$$

in which $N_p(\theta)$ is the number of object pairs with an angular separation in the bin centered on θ with width $\delta\theta$, and $N_r(\theta)$ is the number of pairs for the same number of objects distributed randomly over the same area. The estimator given by (13) is used to compute the angular correlation function for (a) the set of objects classified as

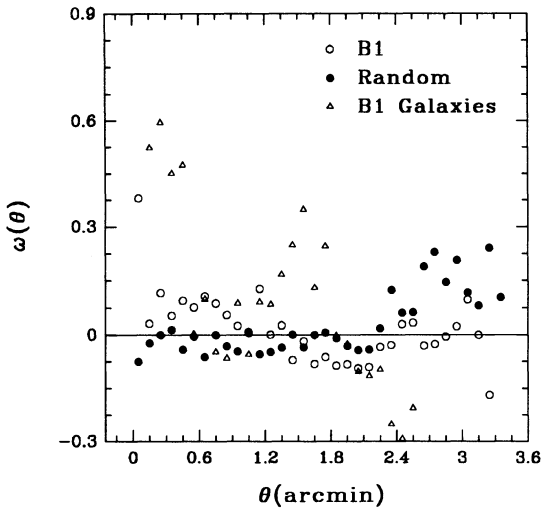

FIG. 4. The angular two-point correlation function $\omega(\theta)$ is calculated for three different data samples, using the Monte Carlo estimator described in the text. Note that our estimate for $\omega(\theta)$ breaks down for $\theta \gtrsim 2'$, since this extent is comparable to the size of the CCD field. The angular correlation function for the 163 objects classified as galaxies (open triangles) from the B1 field shows weak evidence for clustering on a scale of 1 to 2 arcmin. The correlation function for the 321 objects classified as starlike (open circles, i.e., the objects defining our B1 background LF) by comparison show a much smaller level of scatter, comparable with a *randomly* distributed sample of the same size (solid dots).

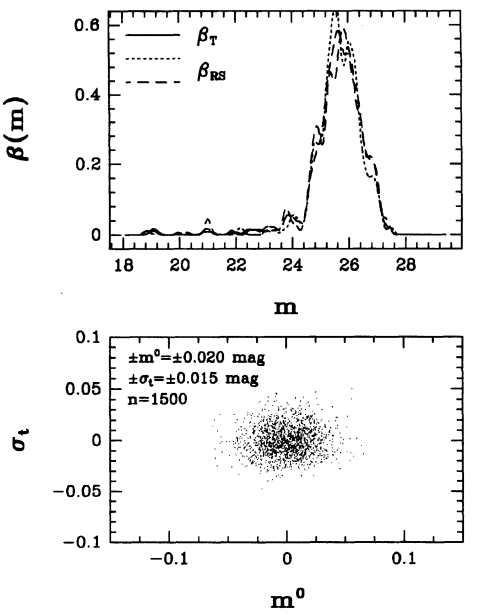

FIG. 5. The results of a simulation to determine the effect of $\pm\sqrt{N}$ variations in the background LF on the GCLF parameters. In the upper plot, β_T represents a "true" β (i.e., we used the combined sample of B1 and B2 fields with a Gaussian dispersion of 0.1 mag to define this β_T), and β_{RS} are two random samples drawn from the "true" LF. The lower plot illustrates the scatter in the estimate of the GCLF intrinsic parameters m^0 and σ_t, as determined from numerical simulations in which the background LF differs randomly by this amount. The scatter on both m^0 and σ_t is negligible compared to the uncertainties arising from the probability contours (below).

galaxies and removed from the B1 field, (b) the unclassified data set for the objects remaining on the B1 frame, and (c) a distribution of 321 objects spread randomly over an area the same as the B1 field. The results are illustrated in Fig. 4; note that the calculated values of $\omega(\theta)$ are not valid for $\theta \gtrsim 2$ (comparable to the size of the CCD field itself). For objects showing no intrinsic clustering, $\omega(\theta)$ should simply oscillate around zero for all θ. As expected, there is some evidence for clustering (on scales of $1' \sim 2'$) of the B1 objects genuinely classified as galaxies. However, the correlation function for the remaining objects (i.e., those classified as starlike) is consistent with the random distribution within the scatter of the data. Thus we are justified in adopting a frame to frame variance that is adequately described by Poisson statistics.

We quantitatively determined the uncertainty in our parameters (m^0, σ_t) due to these realistic background LF fluctuations by performing the following Monte Carlo simulation. The master background LF $\beta(m)$ calculated from the combined B1B2 field was used as a template to generate 1500 random samples, with the number of objects equal to $320 \pm \sqrt{320}$, with the Poisson uncertainty limit justified above. These 1500 artificial samples then mimic the expected variations in the background LF between neighboring fields in the Virgo Cluster (i.e., varying both the number of objects and the shape of the LF). To each of these 1500 random background vectors we then added the same GCLF of size 500 data points, randomly drawn from a t_5 distribution of peak $m^0 = 23.5$ and dispersion $\sigma_t = 1.2$. Then, our maximum-likelihood code was employed to estimate the peak and dispersion for this GCLF, and these estimates were plotted on a parameter space scatter plot (Fig. 5). In this manner, all of the variability was confined to the background LF. From the amount of scatter in Fig. 5, we determine that the 68% uncertainties *due solely to the variations in the background LF* are ± 0.020 mag in m^0 and ± 0.015 mag in σ_t. It is clear then that our parameter estimations are robust to statistical fluctuations in the background, which are disregarded in what follows.

In the preceding discussion we have outlined a new maximum-likelihood method to estimate the GCLF intrinsic parameters, based upon a more exact formulation of the observed LF. But are the resulting parameter solutions systematically correct? As a consistency check, we must first compare our results to the previous solution of HAPV; this comparison will be done in Sec. 5. Of equal importance, we must perform simulations to look for any bias in the results.

To perform these simulations, we generate a random GCLF, consisting of a set of $N = 600$ data points, drawn from a t_5 distribution of known peak and dispersion. Incompleteness is accounted for by a simple step function (i.e., the completeness drops suddenly from unity to zero at the chosen limiting magnitude m_ℓ), such that the randomly generated GCLFs are truncated by removing all

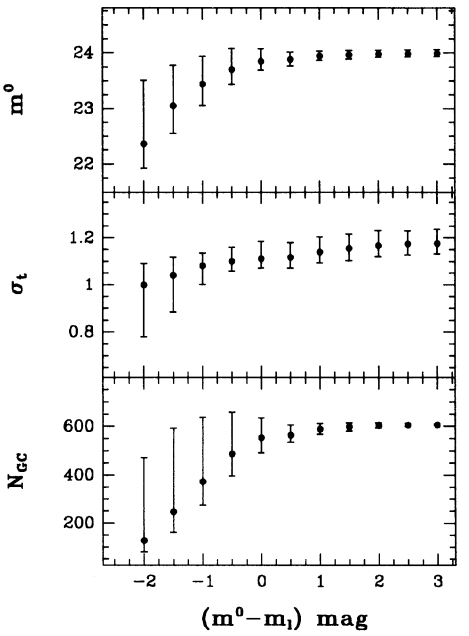

FIG. 6. The results of the simulations designed to detect the bias which results when using the maximum-likelihood parameter estimation techniques on a magnitude-limited data set. Each point in this plot represents the median of 1000 simulations, and the error bars encompass 34% of the data on each side of this median. The median was used instead of the mean, because of the extremely skewed nature of the simulations in the region $(m^0-m_\ell)<0$. We suspect that the indent noticeable at $(m^0-m_\ell)=0.5$ in all three plots is an artifact, caused by deviations from a perfect t_5 distribution in the randomly generated GCLF.

data points fainter than m_ℓ. This GCLF is then added to the background *LF* from field B2, similarly truncated. Then, Eqs. (6) and (7) are solved for $\hat{m}^0$ and $\hat{\sigma}_t$ with K held constant [i.e., the K value was determined from (8) using the number of data points in the incomplete GCLF and the number of points in the B2 field]. Finally, the adopted cutoff m_ℓ is varied and the solutions repeated to determine any mean bias as a function of m_ℓ.

The results of these simulations are presented in Fig. 6. Each point in this figure represents the median of 1000 simulations, and the error bars represent the 68 percent probability range on this median. Note on this figure that a bias towards a brighter peak and a smaller dispersion becomes appreciable if the limiting magnitude m_ℓ is *brighter* than GCLF turnover, (i.e., $m^0-m_\ell \lesssim 0$). Contrarily, if the data do reach to the turnover point or fainter, then systematically correct answers are obtained to within the random uncertainties of the solution. It is clear from Fig. 6 that the biases in the parameters are correlated; this effect was noted in the earlier study of Hanes & Whittaker (1987) and in the restricted least-squares formulation by Harris (1988), and is also seen more dramatically in the probability contour plots to be shown below. Harris (1988) used his simulation to set an effective upper limit on the distance range for the GCLF as a standard candle.

Our simulations, as well as the other two mentioned above, suggest in total that it is necessary to observe the GCLF at least to a limit of $m_\ell \simeq m_0$, and preferably deeper, for the parameter solution to yield unbiased results. As all three studies demonstrate, this effect seems to hold regardless of the particular functional fitting method used. In the case where m_ℓ falls significantly short of m_0, the most obvious way to avoid bias is to *assume* a value for the dispersion σ_t from external considerations and to solve for m_0 alone (see Harris 1988). For our analysis of the Virgo data, we deal with the detected bias by simply correcting for it (i.e., there is less of an error introduced by correcting for this well-defined bias than is introduced by assuming a most-likely wrong value for the dispersion). Our correction factor is calculated as the difference between the mean of the simulations and the true value of the parameter, for the case of $(m^0-m_\ell)=0.5$ mag, which closely represents the HAPV data limits. This correction yields the same results as a two-pass solution (i.e., a method in which the estimate for σ_t is bias corrected, and then held constant as the maximum-likelihood solution for the bias corrected peak, m^0, is found). The (small) resulting correction factors as deduced from our simulations are $\hat{\sigma}_t/\sigma_t=(1.1171/1.2)=0.9309$, $\hat{m}^0/m^0=(23.8852/24.0)=0.9952$, and $\hat{N}_{GC}/N_{GC}=(565/600)=0.9417$. In the graphs presented in the next section, the probability contours are correctly shifted in parameter space by these amounts.

5. RESULTS FOR THE VIRGO GALAXIES

We first perform our calculations for the three Virgo galaxies in such a way that we can directly compare our new method with that of HAPV. To do this, we employ exactly the same input material: a Gaussian distribution function for $\gamma(m)$, the same combination background B1B2 for all three galaxy fields, and no adjustment for the intrinsic bias described above. We performed the calculations as described in Sec. 3, and obtained the maximum-likelihood probability contours for B^0 and σ_G, illustrated in Fig. 7. These two-dimensional contours are collapsed to two one-dimensional probability densities by integrating over the second coordinate. The parameter estimates and their associated uncertainties are thus calculated by finding the parameter limits around the one-dimensional peak which enclose 68% of the total area. (For this reason, the one-dimensional uncertainties are smaller than the corresponding two-dimensional uncertainties that would be read directly from the contour plots; an additional minor difference occurs because of contour asymmetry along a given axis). These results, together with the results obtained by HAPV, are listed in Table 4. Within the statistical uncertainties, our results are consistent with those by HAPV.

For our final parameter estimation, we now switch to the t_5 formulation for the $\gamma(m)$ function, and solve Eq. (1) for three separate combinations of galaxy and background fields: NGC 4365 and B1, NGC 4649 and B2, and NGC 4472 and B1B2. Though no significant difference would result in using the combination background B1B2 for all three (see HAPV for a discussion of the internal agreement

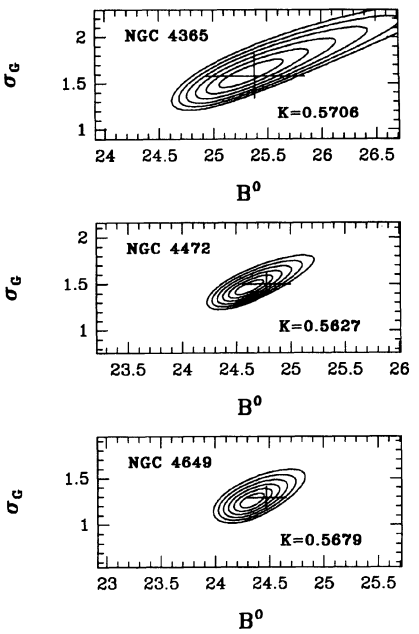

FIG. 7. Our GCLF estimates compared with HAPV's previous results. Here, maximum-likelihood probability contours are generated for a Gaussian GCLF, and the combined background B1B2 for all three galaxies. The most probable GCLF parameter estimates by maximum-likelihood (not bias corrected) are at the centers of the contour plots. The contour lines represent, from inner to outer, the 0.5, 1.0, 1.5, 2.0, 2.5, and 3.0 standard deviation probability limits. The two-dimensional maximums for the contours, from top to bottom, are (25.311, 1.592), (24.611, 1.458), and (24.316, 1.249); note that these values are slightly different from the one-dimensional values quoted in Table 1, for reasons discussed in Sec. 5.1. The results obtained by HAPV are represented by the superimposed straight lines, with lengths equal to their 1σ uncertainties.

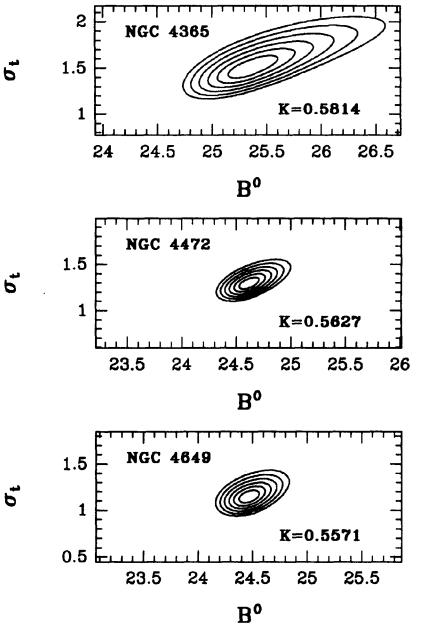

FIG. 8. The maximum-likelihood probability contours for the GCLF parameters in the three Virgo giant elliptical galaxies. These contours have been bias corrected. They represent, from inner to outer, the 0.5, 1.0, 1.5, 2.0, 2.5, and 3.0 standard deviation probability limits on the maximum-likelihood best estimates. The two-dimensional maximums for the contours, from top to bottom, are (25.329, 1.467), (24.613, 1.293), and (24.464, 1.146). Note the increased size (lower precision) of the contours for NGC 4365 caused by its increased distance and the subsequently smaller number of observed GCs.

between them), we choose here for NGC 4365 and 4649 to use only the background field nearest to the galaxy.

The probability contour plots in (B_0, σ_t) for the three Virgo giant elliptical galaxies are illustrated in Fig. 8. These contours have been bias-corrected, but the contours do not include the minimal uncertainty which arises due to the $\pm\sqrt{N}$ background variations as discussed above. The two-dimensional contour plots are collapsed to one dimension by integrating numerically along each axis as before, yielding the central values and uncertainties given in Table 5. Inspection of the contour plots in Figs. 7 and 8 shows strong resemblance, which is to be expected since the t_5 and the Gaussian are similar distribution functions and the background fields have very similar shapes. It is, however, also noticeable that the contours in Fig. 8 are more compact (i.e., the parameter solutions are more precise) than in Fig. 7. This is a result first noticed by Secker (1992); the t_5 distribution function, with the power-law fall-off in its wings, is more robust than the Gaussian to outlying data points and therefore a more precise estimator of the GCLF peak.

Two additional points concerning Fig. 8 deserve comment. First, a comparison of Table 1 with Fig. 8 illustrates that the dominant factor in determining the precision of the parameter estimation is the number of data points, whether in the maximum-likelihood approach or the tra-

TABLE 4. Comparison of GCLF parameter estimates for the Virgo gEs.

Galaxy	HAPV's Results		This Paper (γ=Gaussian)		
	B^0	σ_G	B^0	σ_G	N_{GC}
NGC 4365	25.38±0.46	1.58±0.24	25.31±0.35	1.61±0.17	481
NGC 4472	24.78±0.22	1.50±0.12	24.61±0.15	1.47±0.08	844
NGC 4649	24.47±0.18	1.29±0.12	24.33±0.13	1.26±0.08	408

TABLE 5. GCLF parameter estimates for the Virgo gEs.

Galaxy	Background	B^0	σ_t	M_V^0
NGC 4365	B1	25.37±0.24	1.52±0.13	−7.12±0.36
NGC 4472	B1B2	24.61±0.09	1.30±0.07	−7.03±0.27
NGC 4649	B2	24.46±0.09	1.15±0.07	−7.18±0.27

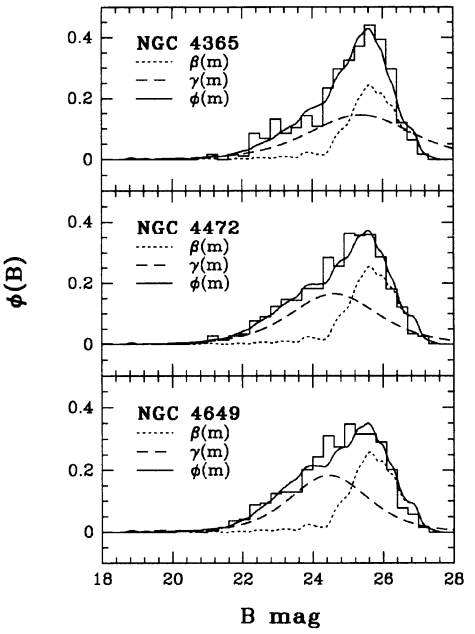

FIG. 9. Illustration of the most probable simultaneous distribution functions $\phi(m)$, as determined from our maximum-likelihood analysis of the data sets. The solid line in each panel represents the solution for $\phi(m)$ in each galaxy field, with the binned GCLF scaled to $\phi(m)$ and plotted on top for comparison. The most probable parameter values are used to plot the background LF $\beta(m)$ and the intrinsic GCLF $\gamma(m)$, which are scaled to $\phi(m)$ by the appropriate values of the mixture proportion constant. Note that it is $\gamma(m)$ and not $I(m)\gamma(m)$ which is plotted, and therefore $\gamma(m)$ is a representation of the GCLF which is predicted by the analysis.

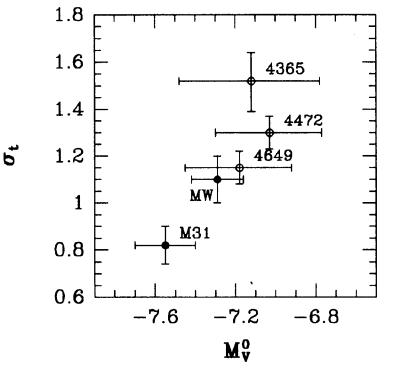

FIG. 10. The GCLF intrinsic parameter estimates (i.e., the absolute magnitude peak M_V^0 and the dispersion σ_t) are plotted for the three Virgo galaxies and for the two Local Group spiral galaxies, as derived in the text. The filled circles are spiral galaxies, and the open circles are the giant elliptical galaxies. Note the apparent correlation between the GCLF peak magnitude and the GCLF dispersion.

ditional least-squares fitting (all other factors like incompleteness being considered equal). The solution for NGC 4365 is thus the least precise of the three, with its decreased number of observed globular clusters being a direct result of its significantly larger distance (see below) which is not compensated for by a fainter limiting magnitude. Second, for all three galaxies the contour plots are strongly tilted with respect to either axis, vividly illustrating the correlation between σ_t and B^0. If $B_l > B_0$, one can solve correctly for the peak and dispersion simultaneously and the uncertainty in the estimate of the peak will approach its theoretical limit of $\sigma_t/\sqrt{N}$ ($\sim \pm 0.1$ mag for $N \gtrsim 300$). However, if $B_l \lesssim B_0$, the estimates for the peak and dispersion become correlated and systematic biases will result. This correlation works in the direction that a fainter peak implies a larger dispersion and a large total population, or vice versa, and it arises because the distribution is not equally well sampled on both sides of the true peak so that the faint half of the GCLF can exert no constraint on the fit (see also the discussion of Hanes and Whittaker). The number of effective boundary conditions is thus reduced from two to one (i.e., the peak and the rapid rise of the GCLF bright side provided sufficient boundary conditions to solve for the dispersion and the peak independently; with only the bright-side rise, the solutions become strongly coupled).

In Fig. 9, we show the final solutions for the distribution functions $\phi(m)$, superimposed upon the *binned* observations. The separate contributions from $\beta(m)$ and $\gamma(m)$ are also plotted to illustrate the total quality of the functional fit.

Finally, we compare the Virgo GCLF turnover luminosities with those of the fiducial Milky Way and M31. For the Virgo data, we convert B to V with a mean globular cluster color $(B-V)=0.69\pm0.03$ (Couture *et al.* 1990, 1991). In addition, we assume a distance modulus for the Virgo Cluster core of $(m-M)_0=30.89\pm0.25$, from Jacoby *et al.* (1992). This distance applies only for NGC 4472 and NGC 4649, since Tonry *et al.* (1990) demonstrate that NGC 4365 is likely to be behind the Virgo core, in the background W cloud. Using their surface brightness fluctuation (SBF) relative distance measurements, we then place NGC 4365 $\simeq$0.9 mag more distant, or at $(m-M)_0 = 31.74\pm0.27$. With a Virgo foreground reddening $E_{B-V} = 0.02$ (Burstein & Heiles 1984), we then obtain $(m-M)_V = 30.95\pm0.25$ (NGC 4472, 4649) and 31.80 ± 0.27 (NGC 4365).

The summarized results for the turnover luminosities M_V^0 and σ_t are listed in Table 5 and plotted in Fig. 10; these supersede the earlier values in HAPV. Notably, the suggestion by Tonry *et al.* that NGC 4365 is actually more distant than was previously thought has brought its estimated GCLF turnover luminosity nicely back into coincidence with the other two central Virgo members and also with M87 (see HAPV). The correlation of Tonry's SBF results and our GCLF results (see also Jacoby *et al.* 1992) provides evidence to support the hypothesis that the range in our estimates for B^0 for the elliptical galaxies is not scatter, but in fact an observable manifestation of structure

within the Virgo cluster. Our new analysis therefore reinforces the conclusion of HAPV that the galaxy-to-galaxy differences in M_V^0(GCLF) are less than 0.2 mag, and certainly small enough to maintain their attraction as a "standard candle."

In Fig. 10, it appears that there may be a systematic difference in the mean (M_V^0, σ) values between the three ellipticals and the two spirals, and perhaps even a general trend for the dispersion to be systematically larger for *fainter* turnover luminosity. The unweighted averages for the GCLF dispersion and peak are $\langle\sigma_t\rangle = 0.96 \pm 0.09$ and $\langle M_V^0\rangle = -7.42 \pm 0.14$ for the spirals and $\langle\sigma_t\rangle = 1.32 \pm 0.09$ and $\langle M_V^0\rangle = -7.11 \pm 0.03$ mag for the ellipticals, or $\Delta M_V^0 = -0.31 \pm 0.33$ and $\Delta\sigma_t = -0.36 \pm 0.13$ (Spiral–Elliptical), implying a fainter GCLF peak and a wider dispersion for the elliptical galaxies. However, with the small number of data points on this graph to date, these conclusions are not of high statistical significance and will need additions from many other galaxies of different types, sizes, and environments to become firm. Nevertheless, to obtain the full *potential* accuracy of ± 0.2–0.3 mag from the GCLF standard candle technique, it would seem appropriate to stick to comparing galaxies of the same morphological type as closely as possible.

This work was supported financially by the Natural Sciences and Engineering Research Council of Canada. Our genuine thanks and appreciation are extended to Robin Ciardullo, Julie Lefebvre, and Chris Pritchet for their many helpful comments and suggestions, support, and enjoyable discussions.

REFERENCES

Burstein, D., & Heiles, C. 1984, ApJS, 54, 33
Couture, J., Harris, W. E., & Allwright, J. W. B. 1990, ApJS, 73, 671
Couture, J., Harris, W. E., & Allwright, J. W. B. 1991, ApJS, 372, 97
Fall, S. M., & Rees, M. 1988, in IAU Symposium No. 126, Globular Cluster Systems in Galaxies, edited by J. Grindlay and A. G. D. Philip (Reidel, Dordrecht), p. 323
Hanes, D. A. 1977, MNRAS, 180, 309
Hanes, D. A., & Whittaker, D. G. 1987, AJ, 94, 906
Harris, W. E. 1986, AJ, 91, 822
Harris, W. E. 1988, in The Extragalactic Distance Scale, ASP Conf. Ser., 4, edited by S. van den Bergh and C. J. Pritchet (Astronomical Society of the Pacific, San Francisco), p. 231
Harris, W. E. 1991, ARA&A, 29, 543
Harris, W. E., & Racine, R. 1979, ARA&A, 17, 241
Harris, W. E., & van den Bergh, S. 1981, AJ, 86, 1627
Harris, W. E., Allwright, J. W. B., Pritchet, C. J., & van den Bergh, S. 1991, ApJS, 276, 491 (HAPV)
Hewett, P. C. 1982, MNRAS, 201, 867
Jacoby, G. H., Branch, D., Ciardullo, R., Davies, R., Harris, W. E., Pierce, M., Pritchet, C. J., Tonry, J. L., & Welch, D. L. 1992, PASP, 104, 599
Peebles, P. J. E. 1980, The Large Scale Structure of the Universe (Princeton University Press, Princeton)
Pritchet, C. J., & van den Bergh, S. 1987, ApJ, 316, 517
Pudritz, R. E., & Harris, W. E. 1993, in preparation
Racine, R., & Harris, W. E. 1992, AJ, 104, 1068
Reed, L. G., Harris, G. L. H., & Harris, W. E. 1992, AJ, 103, 824
Searle, L., & Zinn, R. 1978, ApJ, 225, 357
Secker, J. 1992, AJ, 104, 1472
Secker, J., & Harris, W. E. 1992, in Globular Cluster-Galaxy Connection, ASP Conf. Ser., edited by J. Brodie and G. Smith (Astron. Soc. of the Pacific, San Francisco)
Steffen, M. 1990, A&A, 239, 443
Stetson, P. B. 1987, PASP, 99, 191
Tonry, J. L., Ajhar, E. A., & Luppino, G. A. 1990, AJ, 100, 1416
van den Bergh, S. 1985, ApJ, 297, 361
van den Bergh, S. 1991, PASP, 103, 1053